

Supporting information: Functional plasmonic nano-circuits with low insertion and propagation losses

Arian Kriesch,^{*,†,‡} Stanley P. Burgos,[‡] Daniel Ploss,[†] Hannes Pfeifer,[†] Harry A. Atwater,[‡] and Ulf Peschel[†]

Institute of Optics, Information and Photonics, Erlangen Graduate School in Advanced Optical Technologies, Friedrich-Alexander-University Erlangen-Nuremberg (FAU) and Max Planck Institute for the Science of Light, 91058 Erlangen, Germany, and Kavli Nanoscience Institute, California Institute of Technology, Pasadena, California 91125, USA

E-mail: arian.kriesch@mpl.mpg.de

Optical setup for far-field characterization

The nano-circuits were positioned with 5 nm xyz precision with a piezo scanning system (Physik Instrumente, PI) and optically characterized with a custom-made optical setup (1) that follows the design published by Banzer et al.¹

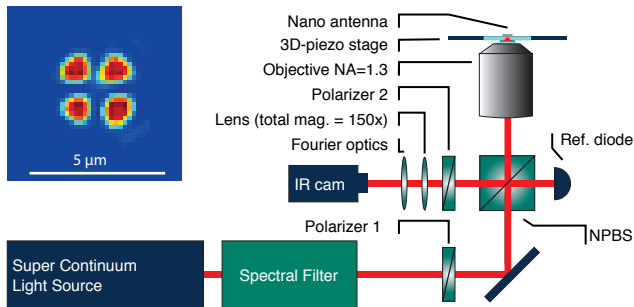


Figure 1: The experimental setup to probe the polarization dependent spectral emission of a nano-plasmonic circuit in real and Fourier space for a broad spectral range $\lambda = 1200\text{ nm}$ to 1850 nm . Inset: The emission from the antenna through crossed polarizers.

The collimated beam from a supercontin-

^{*}To whom correspondence should be addressed

[†]University of Erlangen

[‡]Caltech

uum light source is spectrally filtered by a programmed acousto-optic tunable filter (operated at $\lambda = 1200 - 1850\text{ nm}$) (NKT Koheras, SuperK Extreme) and is subsequently directed through a polarization filter (1) and a non-polarizing beam splitter (NPBS), that directs 50% of the power to a reference diode (InGaAs). The main beam is focused with a high NA objective (NA = 0.9 from air and NA = 1.3 immersion, from substrate) that was carefully characterized to preserve the polarization properties of the laser beam. The diameter of the collimated beam was carefully measured ($FWHM = 1.6\text{ mm}$) with an InGaAs camera and the effective numeric aperture of the experimental focal spot was determined for all subsequent evaluation steps. The focus of the objective is adjusted on the investigated excitation nano-antenna.

At the same time, the objective images the complete nano-circuit, including the emission from the other antennas. The collimated beam, carrying the image, is polarization filtered (polarizer 2) and passes imaging optics to form a real image on an InGaAs NIR CCD camera (Xenics XS, 320 x 256 pixels). The setup features a variable magnification factor (150x, 300x) and an additional, switchable focusing unit to allow for Fourier plane imaging.

By adjusting the polarization filter (2) perpendicular to polarization filter (1), the reflection of

the incident beam is mostly cancelled in the image (1 : 5000 – 1 : 10000 extinction ratio) and the emission from the monitor antennas of the circuit, which are 90° turned with respect to the excitation antenna, can be measured with exceptionally high aspect ratio and dynamic range. However, conversion of field components in the highly focused beam into the perpendicular polarization causes a characteristic four-lobe-pattern that remains intact even when the incident beam is focused on an antenna with no fabrication errors (1 inset). This four-lobe pattern is visible in all measurements at the position of the incoupling antenna (Fig. 7d,e,f of the letter).

The absolute transmission of the nano-circuits was determined by normalization with the known reflectivity of the sample substrate. The spot intensity of the monitor antennas (Fig. 7b of the letter, green circles) was integrated. For each measurement picture for a certain wavelength and circuit, a reference image was taken, featuring the pure reflection of the four-lobe pattern on the substrate. Quasi-analytically, the reflectivity of a silica-to-air interface was calculated by developing a focused Gaussian beam with the correct NA into plane waves, taking into account the crossed second polarization filter.

Possible fluctuations of the probe laser between the main and the reference measurement are eliminated with the reference diode (1). This method of absolute normalization eliminates sources for additional measurement errors and cancels dispersion and loss of the optical setup.

Leakage microscopy

The guided mode of the waveguides does intrinsically not emit into the far-field. However, every waveguide has slight imperfections. Utilizing the high dynamic range of the optical far-field setup, it is possible to image the plasmonic nano-circuit with leakage-microscopy. Highly overexposed ($> 300\times$ saturation intensity) images of a circuit, featuring a directional coupler (ODC) in a direct overlay with an SEM of the same structure show beating patterns inside the waveguides and the coupler.

However, for this high exposure, even the ref-

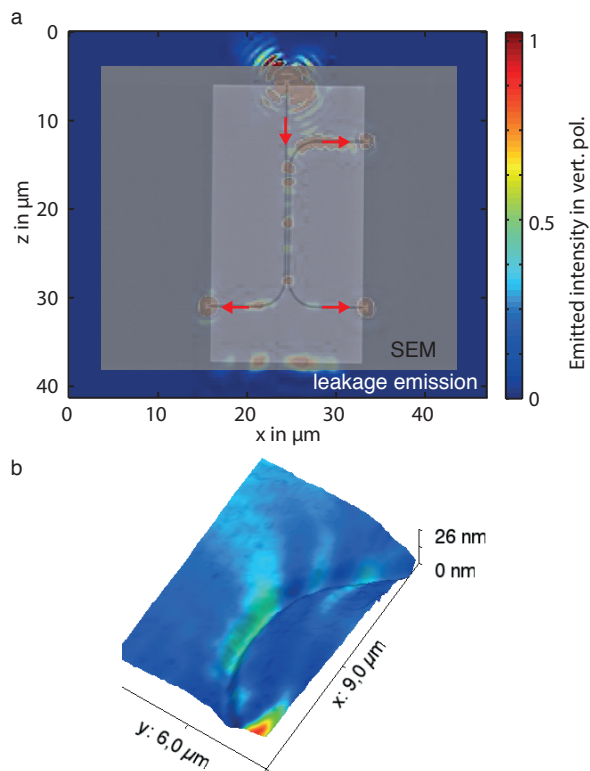


Figure 2: Leakage microscopy of the emission from a nanocircuit with a directional coupler in the configuration with crossed polarizers ($5000 \leq$ suppression ≤ 10000). Highly ($> 300\times$ saturation intensity) overexposed, this real-plane image shows strongly saturated emission from the incident (top) and monitor (left, right) antennas.

erence antenna (compare to Fig. 7b, blue) shows some emission. The slight scattering at the lower edge of the circuit metal pad indicates that slight residual bend loss is due to the conversion into planar SPPs. These subsequently propagate along the metal surface, are scattered out at the lower edge and detected with very high efficiency due to their polarization being parallel to the emission polarization of the monitor antennas.

Near Field Optical Scanning Microscope

The near field scanning optical microscopy (NSOM) measurements (Fig. 4b) were taken with a custom made setup for polarization-adjusted coupling into the optical antennas, based on a modified commercial fiber aperture NSOM system (Nanonics MV 4000).

With tapping, phase-controlled AFM feedback, a $\varnothing \approx 270$ nm Au/Cr coated, FIB processed fiber aperture tip was raster-scanned across the area around the antenna ($10 \times 10 \mu\text{m}$) with 40 nm lateral scan resolution. The near-field, collected from the structure and converted into a propagating mode of an optical fiber, was detected with a high sensitivity, highly amplified InGaAs diode detector.

To reveal the guided mode inside the connected waveguide the scanned intensity is displayed with log-scale and saturation at the beam position was accepted. The plane of scanning is leveled 320 nm above the upper metal boundary due to the cladding spin-on glass (SOG) layer, which in the topography channel of the NSOM still showed smoothed variations of height within $\Delta z \approx 20$ nm that are caused by the underlying $\Delta z \approx 220$ nm topography of the metal structures. In this measurement already little maladjustment of the laser focus leads to slight diffraction artifacts towards the metal surface. To ensure precise adjustment, during the scan also the reflected light from the antenna was collected through the excitation optical pathway and monitored to quantify the distortion of the reflected signal by the scanning NSOM tip.

Additional measurements showed low additional loss from waveguide bends with at least $R = 3 \mu\text{m}$ bend radius (Fig. S2b), which coincides well with the far-field circuit characterization that indicated

these bends to be applicable with negligible additional loss compared to the straight waveguide propagation loss.

Fitting the circuit transmission with a lossy Fabry-Pérot model

Based on the lumped network circuit model² (Fig. 7a) the nano-circuit was treated as a Fabry-Pérot resonator to determine waveguide and antenna properties in one iterative least-square fit over the independent variables wavelength and waveguide length. The fitted model is based on the transmission of a Fabry-Pérot resonator with loss in the resonator and at the mirrors, which has length L and a characteristic wave number k

$$T_{\text{FPR}} = \frac{T_{\text{ant}}}{1 + \Gamma \sin^2(kL)},$$

where T_{ant} represents the efficiency of the antennas to couple the focused laser beam into the FPR cavity, respectively out of it. The antennas are assumed to experience Lorentzian broadening due to plasmonic loss:

$$T_{\text{ant}} = \frac{T_{\text{ant}}^{\text{max}}}{1 + \left(\frac{\lambda - \lambda_0}{\gamma}\right)^2}.$$

Γ determines the inverse line width that can be expressed in terms of the reflectivity $R = R_{\text{in}} = R_{\text{out}}$ of the resonator mirrors, which is caused by imperfect impedance matching between the optical antennas and the waveguides

$$\Gamma = \frac{4R e^{-\alpha L}}{(1 - R e^{-\alpha L})^2}.$$

The antenna efficiency curve and the antenna loss curve are caused by the same loss mechanism. Hence, the reflectivity of the antenna resonator mirrors can be described as

$$\begin{aligned} R &= 1 - T_{\text{ant}} - A_{\text{ant}} \\ &= 1 - \frac{T_{\text{ant}}^{\text{max}} + A_{\text{ant}}^{\text{max}}}{1 + \left(\frac{\lambda - \lambda_0}{\gamma}\right)^2} \end{aligned}$$

where, according to the applied model, A_{ant} represents the absorption inside the antenna with $A =$

$1 - T - R$. With an iterative fit of this model to the experimental circuit transmission values, the spectral propagation length L_0 , the effective index of the guided mode ($n_{\text{eff}} = k\lambda_0/(2\pi)$), the antenna efficiency $T_{\text{ant}}^{\text{max}}$, the central wavelength λ_0 and antenna linewidth FWHM $= 2\gamma$ are determined as free parameters. There may be additional sources for loss, which we are not able to systematically determine.

We can however determine an upper bound for the loss $A \leq 1 - T_{\text{min}} - R$, which effectively makes $T_{\text{ant}}(\lambda)$ a lower bound for the spectral transmission efficiency of the antennas to convert light from the far field into the waveguide and vice versa. Error propagation was applied to all determined free variables $T_{\text{ant}}^{\text{max}}, \gamma, \lambda_0, L_0, n_{\text{eff}}$, based on the error bounds from the iterative fit over several measurements and different fabricated structures. The determined values for the standard deviation σ , as indicated in Fig. 2b, 5a and 5b therefore include statistical errors of fabrication and measurement.

Fitting the optical directional coupler transmission model

The directional couplers are well described with coupled mode theory. The coupling length L_c for periodic full transfer of the power from one waveguide to the other was determined by fitting this model to experimental data over a variation of the parallel length of the couplers $L = 0, 3, 6, 9, 12 \mu\text{m}$. The system is well described as a weakly coupled system of two harmonic oscillators, exchanging energy proportional to the coupling constant κ . The intensity out of the waveguides bar and cross after an ODC of length L is given by

$$I_{\text{bar}} = \cos^2(\kappa L) \text{ and } I_{\text{cross}} = \sin^2(\kappa L)$$

and the coupling length can be expressed as $L_c = \pi/2\kappa$. We used the ratio of the integrated emission from both spots of the monitor antennas (Fig. 7b green, compare Fig. 7 d,e,f) $I_{\text{cross}}/I_{\text{bar}}$ as it is intrinsically more robust to measurement error and even slight maladjustments of the exciting laser beam. However, $I_{\text{cross}}/I_{\text{bar}} = \tan^2(\kappa L)$ diverges and is unsuitable for iterative least-square fitting. A more suitable approach was chosen by

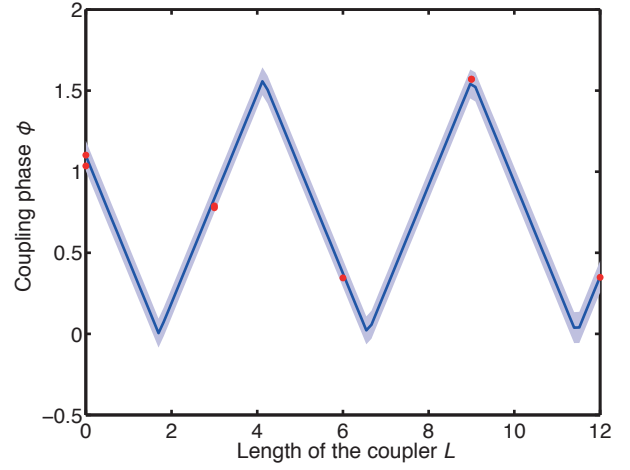


Figure 3: The experimental coupling ratio of 8 nano-circuits with directional couplers of varied straight length L (all $w = 50 \text{ nm}$) is converted to the periodic coupling phase (red dots) and is iteratively fitted with coupled mode theory. Fit result (blue curve) and 90% confidence intervals (blue shaded).

fitting the non-diverging coupling phase, which is as well periodic with full coupling lengths:

$$\begin{aligned} \varphi(L) &= \arctan\left(\frac{I_{\text{cross}}}{I_{\text{bar}}}\right) \\ &= \left| \left[\pi \frac{L - L_{\text{bend}}}{2L_c} \right]_{\text{mod}} - \frac{\pi}{2} \right| \end{aligned}$$

This expression allows for a fit over a variation of the length of the coupler L . L_{bend} represents an additional offset, which is caused by coupling that already occurs in the bends where cross and bar waveguides approach with a radius of $R = 3 \mu\text{m}$. This bend-coupling is expressed in terms of an extra virtual length of the coupler and leads to significant transfer of energy even in the case of zero straight parallel length of the ODC ($L = 0$).

The investigated circuits with the lengths available already cycle through several full coupling lengths. The ODCs with the most narrow filament ($w = 50 \text{ nm}$) resulted in the best fits with least statistical fabrication and measurement deviations and the shortest coupling length, as displayed in Fig. S3. In this case eight measurements on different fabricated circuits were combined. The resulting fit is displayed with 90% prediction bands and gave $L_c = 2.46 \pm 0.04 \mu\text{m}$ coupling length and

$L_{\text{bend}} = 1.7 \pm 0.07 \mu\text{m}$ equivalent coupler length of the bend. The indicated error margins take account for statistical errors, not potential systematic errors that might not have been possible to determine with the applied methods.

Simulation with FDTD and particle swarm optimization (PSO)

The antennas, waveguides and couplers were simulated with a 2D and full 3D Finite Difference Time Domain solver (Lumerical FDTD Solutions). For design purposes, literature values from Johnson and Christy³ were used as material parameters. After first fabricated structures were experimentally characterized, the simulations were repeated with the ellipsometrically determined dielectric susceptibility of Au, which turned out to be close to the initially used literature values in the real part of the dielectric susceptibility, but deviated up to a factor of 1.5 in the imaginary part.

In the simulations, the antenna was excited with a highly focused Gaussian beam with the same beam properties as determined for the experiment with the objectives in use (NA = 0.9 from air and NA = 1.3 from silica). Its emission directionality and efficiency were analyzed in reverse configuration, exciting the guided mode inside the SPP gap waveguide with a mode solver and observing the emission with appropriate frequency domain ports. The more narrow resulting angular directivity of the such optimized antennas was experimentally taken into account by adjusting the collimated beam diameter to slightly reduce the numeric aperture and was characterized as described in section 1.

The supplementary video shows the electric field $|E|^2$ in time domain, as a focused beam (NA = 0.9) impinges the optimized geometry of a Yagi-Uda nano-antenna and is converted into a guided mode, propagating along the waveguide.

Instrumentation

All investigated nano-circuits were fabricated with a lift-off patterning process as described in the main article. A 100 kV Leica EBPG-

5000+ system with pattern generator transferred the nano-circuit designs to the resist. Standard procedures for development, lift-off and standard manufacturer-recipes were used for the application, baking and curing under N_2 atmosphere of the commercially available silsesquioxane spin-on-glass (SOG) Filmtronics 400F. For cross-sections, geometric characterization and fabrication optimization a Zeiss Dual Beam FIB system and a FEI Nova-200 FIB system were used. The laser for far-field and near-field measurements was a NKT Photonics / Koheras SuperK Extreme supercontinuum source with nominal 6W output power and subsequent NKT Koheras acousto-optical tunable filters (AOTFs) for tunable wavelength-selection. A sensitive InGaAs NIR camera (Xenics CS, 320×256) pixels was used for image acquisition of the light emitted from the circuits.

References

- (1) Banzer, P.; Peschel, U.; Quabis, S.; Leuchs, G. *Opt. Express* **2010**, *18*, 10905–10923.
- (2) Engheta, N. *Science* **2007**, *317*, 1698–702.
- (3) Johnson, P. B.; Christy, R. W. *Phys. Rev. B* **1972**, *6*, 4370–4379.